Journal of Materials Chemistry A

ROYAL SOCIETY OF CHEMISTRY

PAPER

View Article Online
View Journal

Cite this: DOI: 10.1039/d6ta01450j

Impact of area scaling on the performance and stability of spin-coated organic solar cells

Angel Sacramento, * Mohamed Samir, Osbel Almora, Amina Shehbaz and Lluis F. Marsal *

Organic solar cells (OSCs) suffer from severe upscaling losses that are predominantly governed by resistive limitations, which hinder efficient lateral charge transport and extraction when reaching the centimeter scale with the current fabrication techniques. In this work, we analyze the impact of area scaling (from 0.09 up to 4 cm^2) on the performance and stability of spin-coated OSCs using PM6:Y7 and PM6:L8-BO in bulk heterojunction architectures. Small-area devices (0.09 cm^2) exhibit PCEs of ~17%, fill factors (FFs) of around 70%, and low series resistances (~1.3 Ω cm^2). When scaling up to 4 cm^2, the open-circuit voltage remains nearly constant, whereas the short-circuit current density and fill factor decrease, resulting in PCEs of 10.7% and 11.1% for PM6:Y7 and PM6:L8-BO, respectively. Atomic force microscopy (AFM) and spatially resolved EQE measurements show that efficiency losses arise mainly from increased series resistance (up to ~10 Ω cm^2) and minor morphological non-uniformities rather than intrinsic limitations of the spin coating process. The stability was also investigated showing PCE losses mainly governed by J_{SC} and FF reductions. PM6:Y7-based devices consistently display superior stability compared to PM6:L8-BO, particularly at larger active areas. These results demonstrate that while efficiency losses upon upscaling are primarily dictated by resistive constraints, the stability of spin-coated OSCs is not compromised at the centimeter scale. Moreover, PM6:Y7-based devices exhibit enhanced stability with increasing area.

Received 16th February 2026
Accepted 26th May 2026

DOI: 10.1039/d6ta01450j

rsc.li/materials-a

Introduction

Organic solar cells (OSCs) have attracted increasing interest as a promising thin-film photovoltaic technology due to their lightweight nature, mechanical flexibility, compatibility with solution processing, and potential for low-cost fabrication over large-areas.[1–4] Spin coating remains the most widely used deposition method in research laboratories, offering simplicity, high reproducibility, and suitability for rapid materials screening and device optimization.[5,6] Promoted by the development of high-performance donor polymers and non-fullerene acceptors (NFAs), laboratory-scale OSCs have recently achieved power conversion efficiencies (PCEs) of over 20%, positioning them among the leading emerging photovoltaic technologies.[7–9]

Despite these advances, a major barrier to technological deployment persists: the substantial performance loss observed when scaling device areas from typical laboratory dimensions (<0.1 cm^2) to larger areas.[10–12] This decrease in efficiency is commonly attributed to non-uniform film formation, increased recombination pathways, and an increase in series resistance (R_S) associated with the finite sheet resistance of indium tin oxide (ITO). These resistive limitations lead to a pronounced reduction in the fill factor (FF) and impose strict constraints on the achievable PCE in large-area OSCs.[11,13] Therefore, a detailed understanding of how device area affects charge transport, spatial uniformity, and operational stability is crucial for the transition from small-area prototypes to large-area photovoltaic modules.[13–15]

While scalable deposition techniques such as blade coating, slot-die coating, and printing are widely recognized as essential for the fabrication of large-area organic solar cells and modules, spin coating remains a reliable and effective deposition method for small-to-intermediate active areas. Numerous high-performance OSCs reported in the literature are fabricated by spin coating, owing to its excellent control over film thickness, morphology, and reproducibility, making it a benchmark technique for materials screening and device optimization.[5] Although spin coating is inherently limited in scalability due to material waste and challenges in achieving uniform coatings over very large substrates, several studies have demonstrated that devices with active areas in the range of approximately 1–10 cm^2 can still exhibit competitive performance and stability when processed by spin coating.[16–18] This intermediate area regime is particularly relevant for understanding performance losses associated with area scaling and for establishing reliable structure–property relationships prior to transitioning to

Department of Electronic, Electric and Automatic Engineering, Universitat Rovira i Virgili, 43007 Tarragona, Spain. E-mail: angel.sacramento@urv.cat; lluis.marsal@urv.cat

scalable deposition methods, which become indispensable in large areas.

In this work, we investigate the impact of active-area scaling-up on the performance and stability of spin-coated OSCs by fabricating devices ranging from 0.09 to 4 cm^2. Two state-of-the-art donor–acceptor systems were employed as the active layer: PM6:Y7 and PM6:L8-BO bulk heterojunctions (BHJs).[19,20] Y7 and L8-BO are high-performance NFAs that enable strong near-infrared absorption, efficient exciton dissociation, and balanced charge transport.[21–24] By comparing these two BHJ systems, we assess how active layer composition influences device scalability under spin-coating conditions. The results provide valuable insights into efficiency losses induced by device area scaling and emphasize the practical limitations of spin coating when transitioning from small-area prototypes to larger-area OSCs. This understanding is crucial for defining the extent to which spin coating remains a viable deposition method before moving toward scalable coating and printing techniques.

Through a combined analysis of photovoltaic performance parameters, AFM-based morphological mapping, EQE-derived photocurrent uniformity, and stability assessments under ISOS-D-1 and ISOS-L-1 protocols,[25] we show that spin coating (Fig. 1d) remains a reliable and effective deposition technique for OSCs with active areas of up to approximately 4 cm^2. The observed reduction in device efficiency at larger areas is therefore not inherent to the spin-coating process itself but instead arises from secondary factors—such as edge-related film instabilities, and increased series resistance associated with large-area architectures. These findings clarify how performance losses evolve with increasing active areas in OSCs and show that scalable coating and printing techniques become necessary mainly due to practical, extrinsic limitations, not because spin coating is inherently unsuitable within this area regime.

Results and discussion

Photovoltaic characteristics obtained by current–density (*J*–*V*) measurements

Conventional OSCs with an architecture of ITO/PEDOT:PSS/active layer/PDINO/Ag were fabricated, where PM6:Y7 and PM6:L8-BO blends were selected as photoactive layers, as shown in Fig. 1d. The chemical structures of PM6, L8-BO, and Y7, are shown in Fig. 1a. The energy level diagrams of the materials are illustrated in Fig. 1c.

The current density–voltage (*J*–*V*) curves of the multiple area OSCs under AM1.5 G illumination (100 mW cm^{-2}) are shown in Fig. S1 (SI), and the photovoltaic performance parameters of the devices based on the PM6:Y7 and PM6:L8-BO blend active layers for the different cell areas are shown in Table 1, which summarizes the average and highest device performance parameters, including the short circuit-current density (J_{SC}), open-circuit voltage (V_{OC}), fill factor (FF), and power conversion efficiency (PCE). It also shows the series and shunt resistances (R_S, and R_{SH}, respectively) extracted from the *J*–*V* characteristics under light. As shown in Table 1, the small area devices (0.09 cm^2) exhibit comparable PCE values of approximately 17% for both active layer systems (PM6:Y7 and PM6:L8-BO), with average V_{OC} values of 841 and 846 mV, J_{SC} values of 27.93 and 28.45 mA cm^{-2}, FF values of 71.80 and 70.18%, R_S values of 1.32 and 1.29 Ω cm^2, and R_{SH} values of 563 and 575 Ω cm^2, respectively.

To place these results in the context of the state of the art, Fig. 1b compares the power conversion efficiency (PCE) of PM6:Y7 and PM6:L8-BO devices as a function of active area with representative literature reports. Both systems exhibit performance values that are fully competitive with previously reported PM6-based organic solar cells across different device areas. In general, literature reports consistently show a reduction in PCE

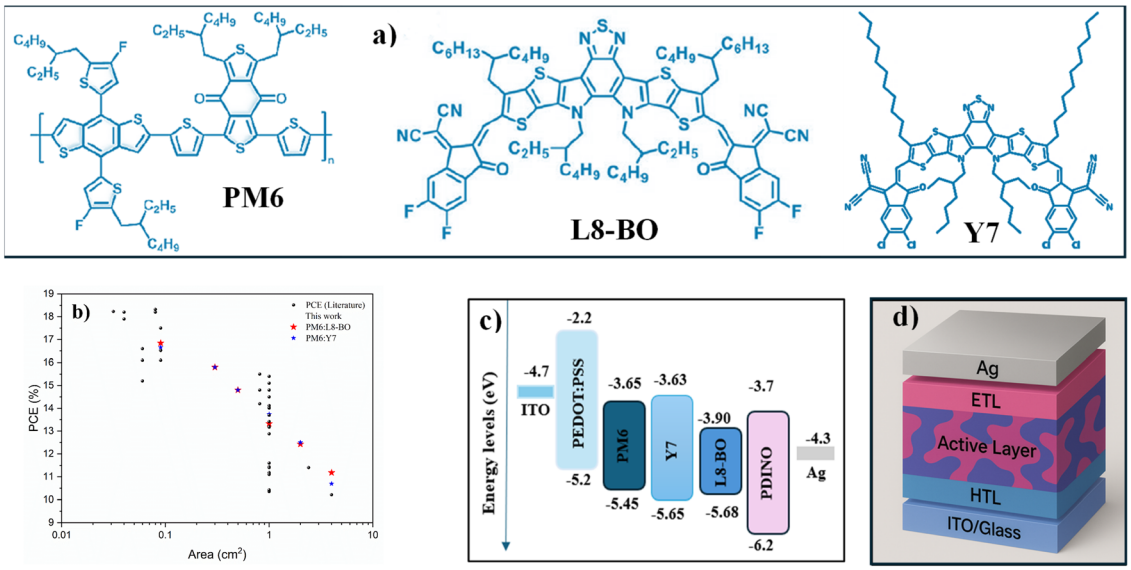

Fig. 1 Molecular structures of the active materials (a) PM6, L8-BO and Y7, (b) PCEs of OSCs with active areas over 4 cm^2 (Table S1, SI), (c) energy level diagram of the OSCs and (d) schematic illustration of the fabricated OSC device architecture.

Table 1 Device performance parameters for PM6:Y7 and PM6:L8-BO OSCs with different areas measured under AM 1.5 G at 100 mW cm^{-2} intensity. All parameters were averaged over twenty devices. The data in parentheses represent the maximum values. The data in square brackets represent integrated J_{SC} calculated from the EQE spectra

Device area cm^2	J_{SC} [mA cm^{-2}]	V_{OC} [mV]	FF [%]	PCE [%]	PCE_{Loss} [%]	R_S [Ω cm^2]	R_{SH} [Ω cm^2]
PM6:L8-BO							
0.09	27.93 (28.62) [27.2]	841 (850)	71.80 (73.00)	16.84 (17.24)	0	1.32 (1.38)	563 (580)
0.29	26.50 (27.65) [26.3]	843 (850)	70.54 (71.25)	15.80 (16.28)	6.2	2.65 (2.81)	551 (565)
0.5	25.20 (26.43) [25.4]	843 (851)	68.45 (69.34)	14.80 (13.50)	12.1	3.97 (4.27)	513 (531)
1	24.84 (25.36) [24.2]	844 (853)	65.42 (67.10)	13.32 (13.71)	20.1	4.45 (4.63)	496 (512)
2	24.50 (25.41) [24.0]	845 (854)	59.56 (61.37)	12.42 (12.80)	26.2	7.35 (7.65)	479 (495)
4	24.20 (24.74) [23.7]	848 (855)	53.77 (54.56)	11.17 (11.37)	33.6	9.70 (10.3)	466 (482)
PM6:Y7							
0.09	28.45 (29.13) [28.3]	846 (853)	70.18 (71.85)	16.65 (17.10)	0	1.29 (1.34)	575 (597)
0.29	27.56 (28.34) [27.7]	845 (851)	69.54 (70.23)	15.85 (15.30)	4.8	2.65 (2.67)	556 (567)
0.5	27.45 (27.68) [27.2]	844 (849)	68.12 (69.03)	14.82 (14.70)	10.9	3.50 (3.70)	538 (552)
1	27.31 (27.49) [27.1]	843 (847)	62.70 (63.72)	13.74 (14.22)	17.5	4.80 (4.92)	525 (537)
2	26.68 (26.85) [25.8]	842 (846)	57.01 (58.75)	12.51 (13.00)	24.8	7.40 (7.59)	511 (526)
4	25.93 (26.55) [25.1]	842 (845)	50.40 (51.34)	10.69 (11.27)	35.8	9.80 (10.5)	479 (497)

with increasing active area, highlighting the critical role of scaling-related losses in organic photovoltaic devices. Notably, the trends observed in this work follow the same general behavior, further supporting the validity of the scaling effects discussed here. The evolution of the performance parameters of the OSCs fabricated with different active layer materials (PM6:Y7 and PM6:L8-BO) as a function of device area is shown in Fig. S2. For completeness, Table S2 summarizes the full photovoltaic parameters for all devices investigated, including different active areas and active layer systems, enabling a direct comparison of device performance across the studied processing and scaling conditions.

As shown in Table 1 and Fig. S2, as the active area is increased from 0.09 to 4 cm^2, distinctive trends are observed in the photovoltaic performance parameters of PM6:Y7 and PM6:L8-BO based OSCs. The V_{OC} remains nearly constant across the entire area range for both active layers, with only minor fluctuations. In contrast, the J_{SC} shows a clear decrease with increasing area, with a more pronounced reduction for PM6:L8-BO devices. The FF decreases almost linearly from approximately 70–71% for 0.09 cm^2 cells to 50–53% for 4 cm^2 devices for both active blends. Consequently, the PCE drops from ~17% to ~11%, with a steeper decrease observed between 0.09 and 1 cm^2 and a more gradual reduction from 2 to 4 cm^2. This behavior correlates with a significant increase in series resistance (from ~1.3 to ~10 Ω cm^2) and a simultaneous decrease in shunt resistance (from ~570 to ~470 Ω cm^2) as the device area increases.

The weak dependence of V_{OC} on device area is consistent with the understanding that V_{OC} in organic solar cells is primarily governed by the energetic offset between the donor HOMO and acceptor LUMO levels, as well as by intrinsic radiative and non-radiative recombination losses, rather than by the lateral dimensions of the device.[26,27] In this context, the slightly lower absolute V_{OC} values observed here compared to state-of-the-art reports can be attributed to differences in material batches, commercial suppliers, and processing conditions, all of which are known to influence donor–acceptor energetic alignment, film microstructure, and non-radiative recombination losses. These results are consistent with studies that have reported that when OSCs are scaled from 0.1 cm^2 to a few cm^2, V_{OC} exhibits only minimal variations, even though other performance parameters decline more significantly.[11,28–30]

The reduction in J_{SC} with increasing device area can be associated with geometrical and resistive constraints on charge collection rather than intrinsic limitations of the photoactive materials. This decrease is mainly attributed to ohmic losses within the ITO anode, which impose field-dependent charge extraction limitations as the device area scales. As lateral transport through the ITO increases, the driving force for charge extraction in regions farther from the collecting electrode is reduced. This, combined with non-uniform current collection and potential edge-related losses, leads to longer carrier residence times. Consequently, bimolecular recombination losses are enhanced before carriers can be successfully collected, even under short-circuit conditions. These effects are consistent with previous studies on large-area OSCs, where non-uniform current distribution and edge-related losses have been identified as key contributors to performance deterioration upon area scaling.[11,18,30–33]

The nearly linear reduction of the FF with increasing active area is primarily associated with the combined effects of increased series resistance and reduced shunt resistance. As the device area increases, longer lateral current collection pathways and the finite sheet resistance of the ITO electrode result in greater resistive losses. In addition, larger device areas increase the probability of localized defects and leakage pathways, which can contribute to a reduction in shunt resistance.[10,33–35]

To further elucidate the origin of the fill factor degradation upon device upscaling, a quantitative analysis based on the characteristic photo-resistance ($R_{Ph} = V_{OC}/J_{SC}$) was performed, following the framework described in the SI. In the absence of ohmic losses, the fill factor is expected to follow its ideal dependence on the normalized photovoltage and ideality factor,

as described by eqn (S2). However, when the parasitic series or shunt resistances approach the magnitude of R_{Ph}, significant deviations from the ideal FF are expected. For the studied devices, R_{Ph} was found to be approximately ~33 Ω cm^2, indicating that FF losses should become significant for R_S > 3 Ω cm^2 and R_{SH} < 300 Ω cm^2. By comparing the experimentally extracted FF values with theoretical predictions[36] considering the isolated effects of R_S and R_{SH} (eqn (S3) and (S4)), it is observed that the FF evolution with increasing active area is accurately reproduced when only series resistance losses and ideality factors are considered, whereas shunt resistance effects alone fail to capture the experimental trend (Fig. 2). This further supports the conclusion that series-resistance-related transport and collection losses constitute the dominant mechanism driving FF degradation upon upscaling, while shunt-related leakage pathways play a secondary role in the present devices.

The dark *J*–*V* measurements and their derivatives provide additional insight into the voltage-dependent resistive behavior of the devices. From the dark *J*–*V* curves (Fig. 3a), the voltage-dependent resistance (Fig. 3b) and the corresponding dark ideality factors (Fig. 3c) were extracted, revealing that both ideality factors and resistance change with applied bias.[37] The dark series resistance R_S remains of the same order as that extracted under illumination and increases with active area, reaching values close to 10 Ωcm^2 for large area devices. In contrast, the shunt resistance in the dark is orders of magnitude higher (approaching ~100 kΩ cm^2) than the photogenerated shunt resistance extracted under illumination. This behavior is consistent with previous observations that dark shunt resistance can scale strongly with device parameters and is indicative of leakage and trapping effects that dominate in the absence of photogenerated carriers, whereas under illumination the effective shunt resistance is limited by additional photocarrier extraction pathways and recombination processes observed in OSCs.[38,39]

Because of the simultaneous reductions in J_{SC} and FF, the PCE decreases noticeably with increasing area. The highest drop in efficiency is observed during the initial scale-up (from 0.09 to 1 cm^2) followed by a more gradual decline at larger areas (see Fig. S2d), which is consistent with literature reports.[28,40–44]

From a mechanistic perspective, this behavior originates from lateral voltage drops within the ITO electrode, which become increasingly significant as the device area increases. The finite sheet resistance of the ITO leads to spatial variations in the local potential across the device, resulting in non-uniform current extraction and a reduction in the effective operating voltage. These lateral resistive effects not only increase ohmic losses, contributing to the observed FF degradation, but also affect charge collection efficiency, thereby impacting J_{SC}.

Overall, the scaling behavior observed in this work is in good agreement with previously reported trends for large-area organic solar cells and highlights that the performance degradation is primarily governed by geometrical–electrical constraints associated with lateral charge transport and electrode conductivity, rather than by intrinsic limitations of the active layer.[42,44–46]

The integrated J_{SC} calculated from the external quantum efficiency (EQE) spectra of devices with different areas shows values with a small difference from the results obtained by the *J*–*V* measurements (Table 1), see Fig. 4. The EQE of 2 cm^2 devices based on PM6:Y7 (Fig. 4c) and PM6:L8-BO (Fig. S3) BHJ OSCs were measured by focusing the light spot (21 mm^2) on nine and three different locations of the effective region, respectively. The shape and intensity of the EQE curves obtained from the different zones of the devices show small variation, indicating good homogeneity of the active layer film. Interestingly, the EQE of the PM6:Y7 device approaches ~100% at ~850 nm, which can be attributed to optical interference effects and reflection from the Ag back electrode, leading to local enhancement of the optical field rather than unity transmittance of the ITO electrode.[47,48] The average integrated J_{SC} obtained from the different zones of the device for PM6:Y7 OSCs was 25.86 mA cm^{-2}, and 24.12 mA cm^{-2} for PM6:L8-BO. These small variations are consistent with the results obtained from atomic force microscopy (AFM) images (see Fig. 5).

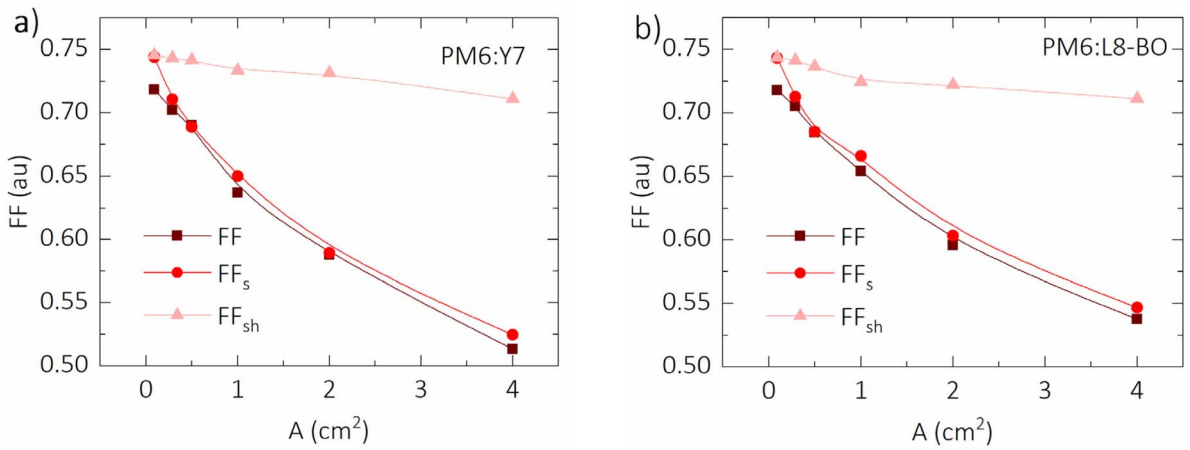

Fig. 2 Evolution of the fill factor as a function of active area for (a) PM6:Y7 and (b) PM6:L8-BO (including the experimental results (FF, squares), and theoretical predictions for parasitic ohmic losses due to sole series resistance (FF_S, circles) and sole shunt resistance (FF_{Sh}, triangles)).

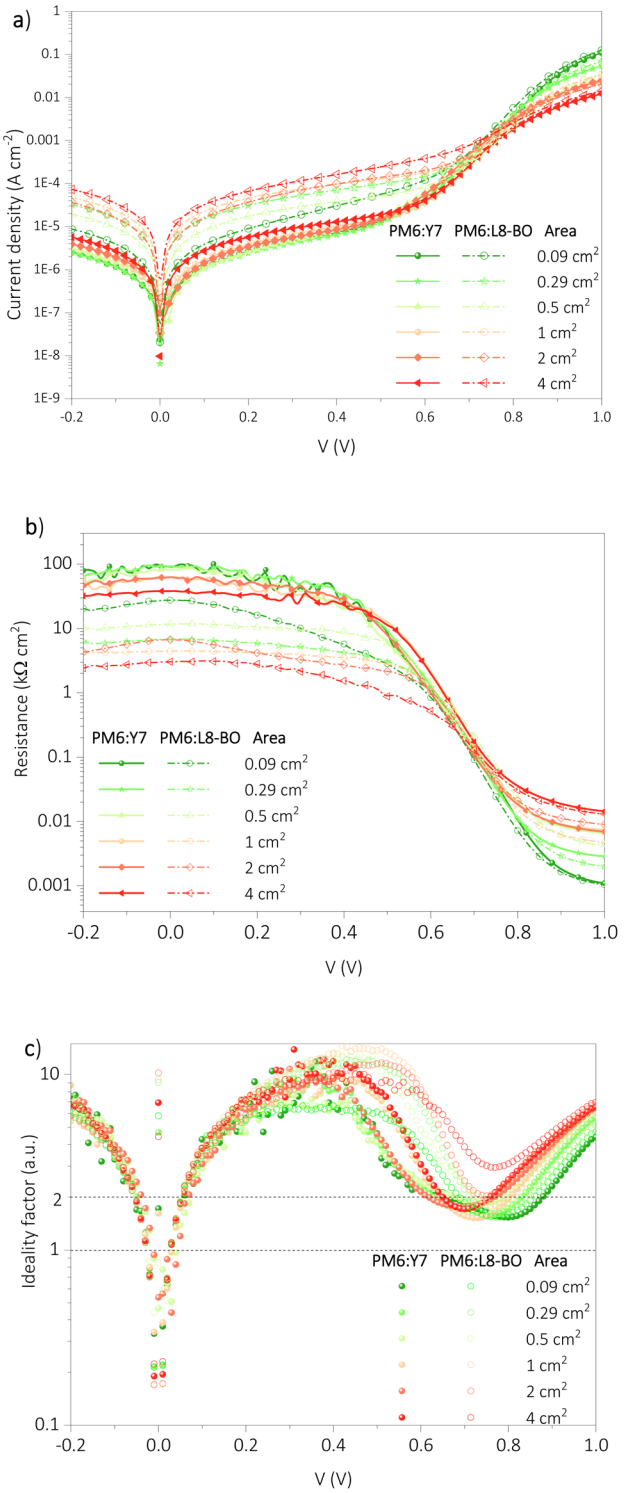

Fig. 3 (a) J–V curves measured in the dark, (b) the dark resistances for different device areas, and (c) the ideality factor derived from dark J–V measurements.

The surface topography of the blend films was examined *via* AFM to assess the influence of the non-fullerene acceptors (L8-BO and Y7), processing solvents (CB and CF), and additives (CN and DIO). Fig. 5 shows AFM topographic images of PM6:L8-BO and PM6:Y7 films deposited on glass/PEDOT:PSS. The PM6:L8-BO films display minimal surface roughness variation, with root mean square (RMS) values of 1.18, 1.24, and 1.28 nm measured in the right, center, and left regions of the substrate, respectively (Fig. 5a–c). In contrast, PM6:Y7 films show higher spatial roughness variations, with RMS values of 2.3, 2.1, and 2.4 nm across the same regions (Fig. 5d–f). These results indicate that both the non-fullerene acceptors (L8-BO and Y7) and the choice of solvent (CB or CF) influence the domain morphology of the blend films, with smoother surfaces observed for CF-based films, which is consistent with reported studies.[49,50] In the case of CB-based films, larger domains were formed, which can slightly limit the formation of an optimal interpenetrating morphology and lead to a slightly lower FF.[51–53]

Therefore, the observed performance reduction in scaled-area devices is not governed by intrinsic limitations in exciton generation or dissociation, but rather by extrinsic, area-dependent losses associated with charge transport and collection. In particular, the increase in series resistance (see Table 1 and Fig. 3a and b) arises predominantly from lateral transport limitations imposed by the finite sheet resistance of the ITO electrode, which lead to spatial variations in the local potential and non-uniform current extraction across the device. These effects reduce the efficiency of charge collection and increase the probability of recombination losses, ultimately contributing to the observed decrease in the EQE-integrated J_{SC} of the upscaled OSCs. Additionally, reduced lateral charge transport efficiency and local inhomogeneities further exacerbate these losses, highlighting the critical role of device geometry and electrode conductivity in limiting performance at larger areas.

To mitigate these scaling-induced losses, both materials optimization and device architecture must be carefully considered. From a materials chemistry perspective, improving charge extraction through interfacial engineering and enhancing electrode conductivity using conductive interlayers or nanostructured additives can help reduce resistive losses and suppress recombination. In parallel, device-level strategies such as incorporating metallic grid structures, integrating highly conductive nanostructures (*e.g.*, Ag nanoparticles or nanowires), or employing narrow stripe geometries with sub-cell widths below ~1 cm can effectively shorten lateral charge collection distances and minimize voltage drops across the device. These approaches directly address the geometrical–electrical constraints identified in this work and provide practical design routes for preserving high performance in large-area organic solar cells.

Stability analysis

To evaluate devices lifetime, we performed two tests: shelf life (ISOS-D-1 protocol) and laboratory simulation (ISOS-L-1 protocol).[25] The device area-dependent lifetime was analyzed to determine its impact on performance degradation and to assess scalability. The operating shelf lifetime (T_{80}) of each studied cell is summarized in Table 2 and Fig. 6f. Fig. 6a and b shows the evolution over time of the normalized PCE according to ISOS D-1, while Fig. 6c and d show the normalized PCE according to ISOS L-1. Fig. S5–S8 present the evolution of the rest of the

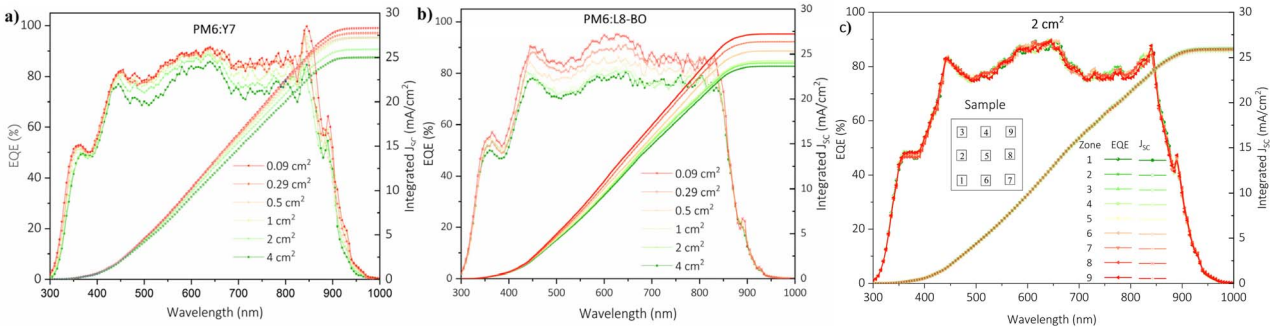

Fig. 4 EQE and calculated J_{SC} for different-area devices (a) PM6:Y7 OSCs (b) PM6:L8-BO OSCs and (c) EQE and calculated J_{SC} obtained from nine different locations of a single 2 cm^2 PM6:Y7 OSC device.

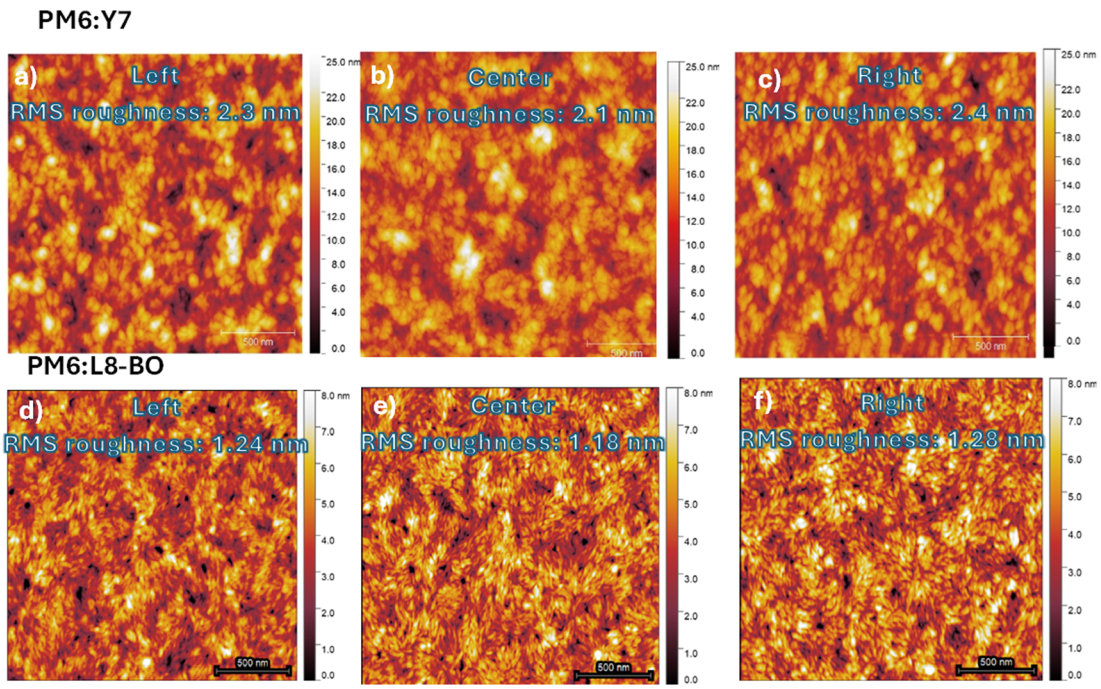

Fig. 5 Atomic force microscope (AFM) images of PM6:Y7 and PM6:L8-BO blends: (a and d) left, (b and e) center, and (c and f) right of each sample, respectively.

normalized performance parameters according to ISOS D-1 and ISOS L-1 protocols for OSCs with PM6:Y7 and PM6:L8-BO.

Shelf life (ISOS-D-1 protocol)

The samples stored under dark conditions were systematically measured under standard 1 sun illumination. The resulting V_{OC} trend exhibits the highest stability among all photovoltaic parameters, remaining above 95% of its initial value after 3000 h, independently of the active area. This behavior is consistent with previous reports on PM6:Y7 and related non-fullerene acceptor (NFA) systems.[22–24,54,55] Several studies have shown that, in the absence of light and oxygen, trap generation and energetic disorder evolve gradually, leading to minimal changes in V_{OC}.[19,56]

The J_{SC} shows only a slight decrease with aging time, typically below 7%, and no strong dependence on device area is observed. Similar weak dark degradation of J_{SC} has been widely reported for high-performance PM6:Y7 devices and has been attributed to acute changes in charge transport and extraction rather than to bulk photoactive layer degradation.[24,57–59]

In contrast, the FF exhibits a more pronounced decay over time and represents the main contributor to the PCE loss under ISOS-D-1 conditions. While FF degradation in OSCs is often associated with an increase in series resistance and a reduction in shunt resistance due to electrical aging of transport layers and interfaces, the extracted Rs and R_{SH} values in our devices show only minor variations with aging time. This suggests that the observed FF decay is not primarily driven by bulk resistive loses, but rather by more subtle interface-related degradation

Table 2 The summary of shelf lifetime data for the non-encapsulated devices under different testing conditions, following the ISOS D-1 and L-1 protocols

Device area (cm^2)	T_{80} ISOS-D-1 PM6:Y7 (h)	T_{80} ISOS-D-1 PM6:L8-BO (h)	T_{80} ISOS-L-1 PM6:Y7 (min)	T_{80} ISOS-L-1 PM6:L8-BO (min)
0.09	2174	1220	376	81
0.29	2280	1296	391	108
0.5	2422	1368	400	125
1	2493	1667	994	151
2	2867	1859	1227	227
4	2913	1915	1268	231

effects, such as changes in charge extraction efficiency, contact selectivity or increased interfacial recombination.[60,61]

In our work, we find that devices with larger active areas exhibit a smaller increase in series resistance, which leads to reduced FF decay. Consequently, these devices show enhanced stability.

Notably, this stabilization effect is particularly evident for PM6:Y7-based devices, which display the lowest FF degradation and the longest T_{80} values. This suggests that the impact of localized weak spots and interfacial defects is statistically averaged over larger device areas.

Laboratory simulation (ISOS-L-1 protocols)

Finally, the long-term stability of the devices was tested in a solar simulator under continuous one sun illumination (AM 1.5 G) under open circuit conditions; all devices exhibit an initial transient regime commonly referred to as burn-in,[62,63] followed by a slower degradation phase. The V_{OC} shows a small initial decrease during the first minutes of illumination and subsequently remains relatively stable over extended periods. This observation matches numerous reports on PM6:Y7 and PM6:L8-BO systems, where photochemical and interfacial degradation processes under controlled conditions induce only minor shifts in V_{OC}, highlighting the relative robustness of the donor–acceptor energetics and interfacial energy alignment. It has been shown that, although light-induced trap states can form during operation, their density is often insufficient to significantly alter the effective bandgap or the non-radiative recombination losses governing V_{OC}.[23,24,64,65]

In contrast, the *PCE* degradation under ISOS-L-1 conditions is primarily governed by the evolution of J_{SC} and FF. The J_{SC} exhibits the largest relative decrease, particularly in PM6:L8-BO devices, indicating that photo-induced processes affecting charge transport and extraction dominate the performance decay. Since V_{OC} remains comparatively stable while both J_{SC} and FF decrease under continuous illumination, the photocurrent loss is more consistently associated with increased recombination and reduced charge collection efficiency than with a dominant loss in built-in potential. In this context, several concurrent mechanisms may contribute to the observed J_{SC} decay, including the formation of photo-induced trap states, increased energetic disorder, gradual disruption of charge percolation pathways, and interfacial degradation affecting carrier extraction. Similar J_{SC}-driven degradation has been reported in Y-series NFA-based OSCs,[66–68] where light-induced trap formation and subtle chemical modifications of the acceptor phase progressively reduce carrier mobility and enhance recombination losses. Sangwan *et al.*[69] reported that UV-induced degradation in Y-series NFAs promotes the formation of shallow trap states associated with reduced carrier mobility and enhanced recombination, while only minor morphological disruption is required to induce substantial photocurrent losses. In addition, broader studies on NFA photodegradation have shown that light-induced chemical modifications and local energetic disorder can progressively impair charge transport and photocurrent generation in Y-series systems. Illumination-induced aggregation of NFAs and the growth of isolated acceptor-rich domains may further disrupt charge percolation pathways and suppress photocurrent generation.[57,70]

The FF also decreases progressively under illumination and closely follows the reduction of shunt resistance. This behaviour is consistent with literature reports linking FF degradation to the accumulation of photo-induced defects and interfacial deterioration, which increase leakage currents and non-radiative recombination losses.[71,72] Importantly, the series resistance does not exhibit a dominant increase under illumination. An initial decrease in R_s is observed, followed by a mild and nearly linear increase that remains close to the initial value.[73] A key finding of this study is that the stability under both dark and illuminated conditions improves with increasing active area. Larger-area devices consistently exhibit longer T_{80} lifetimes and slower degradation rates, despite their lower initial efficiencies, as is shown in Fig. 6e and f.

To verify whether the apparent improvement in stability with increasing device area could arise solely from differences in the initial device performance, the PCE evolution was also analyzed in absolute terms (Fig. S4). In both material systems, the degradation curves do not overlap when expressed in absolute values and cannot be superimposed by a horizontal shift along the time axis, indicating that the observed stability trends are not solely determined by differences in the initial performance. Under ISOS-D-1 conditions, all devices exhibit similar degradation profiles, with slightly steeper slopes for smaller-area devices. Under ISOS-L-1 conditions, more pronounced differences are observed, with smaller-area devices displaying a stronger burn-in and faster early-stage decay, whereas larger-

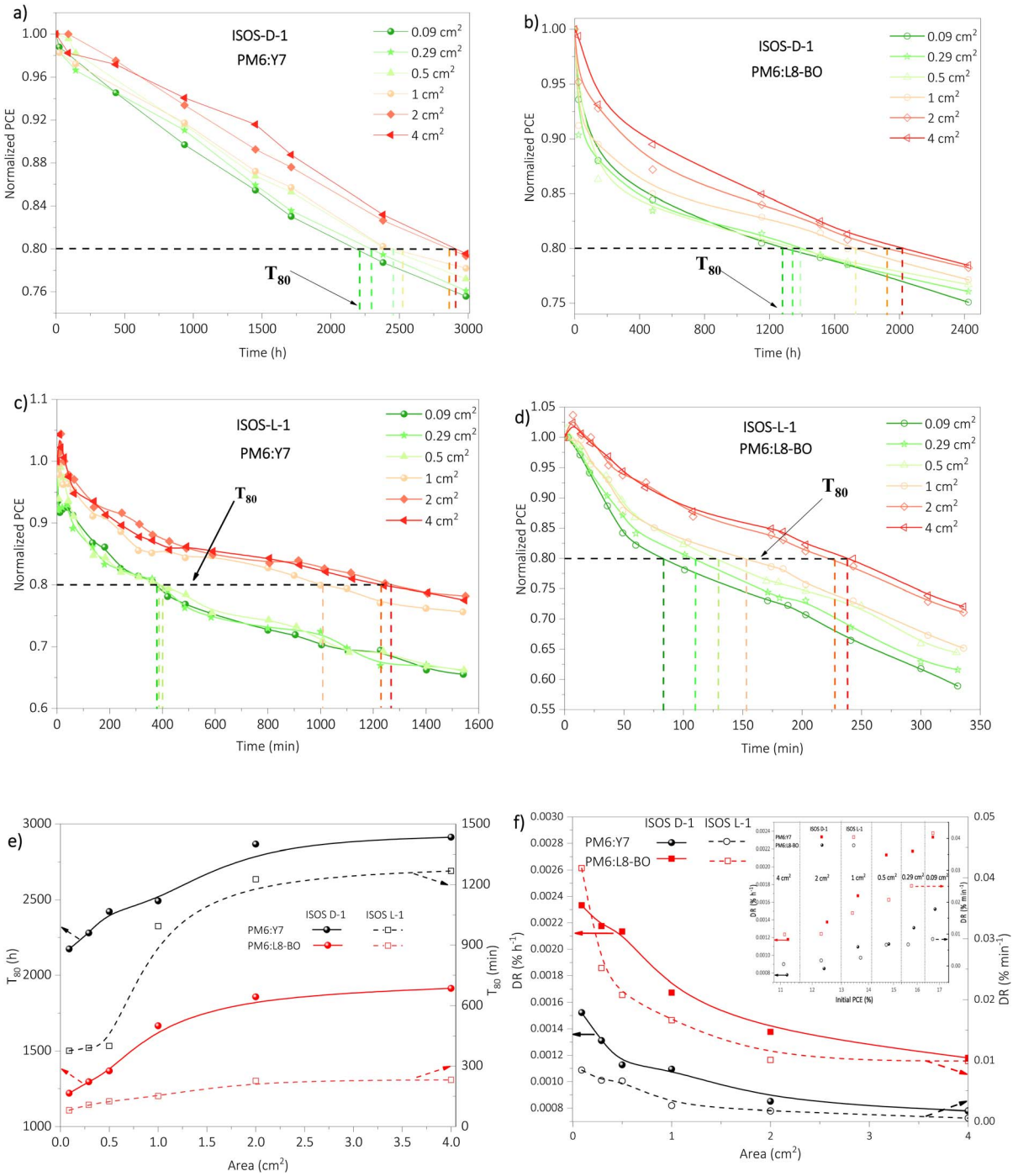

Fig. 6 Normalized PCE over time for each device area with PM6:Y7 and PM6:L8-BO active layers under dark and continuous illumination following the ISOS-D-1 (a and b) and ISOS L-1 protocols (c and d), (e) T_{80} *vs.* area, and (f) degradation rates *vs.* area (inset DR *vs.* PCE_initial for each device area).

area devices show a more gradual evolution. These results confirm that the apparent stability improvement with increasing area is not an artifact of normalization but reflects an area-dependent modulation of the degradation dynamics.

Area-dependent effects on performance and stability have been previously reported in organic solar cells, particularly when transitioning from small-area laboratory devices to larger-area cells or modules. Several studies have shown that degradation in OSCs is often spatially inhomogeneous and dominated by localized failure pathways, such as edge-related defects, interfacial degradation, and non-uniform ingress of oxygen and moisture, which tend to initiate at the device perimeter rather than uniformly across the active layer.[74,75] Consequently, small area devices, characterized by a higher

perimeter-to-area ratio, are more strongly affected by edge-driven degradation mechanisms, leading to faster apparent performance losses under similar stress conditions. In contrast, larger-area devices exhibit less relative perimeter exposure, which effectively diminishes the impact of edge-related environmental stress, resulting in a slower degradation rate under comparable aging protocols.[74,76] This geometric effect provides a plausible explanation for the improved stability observed for larger-area devices in this work and suggests that the apparent area-dependent stability arises from statistical and geometric average of localized degradation processes, rather than from an intrinsic improvement of the materials or interface stability.

The stability test results can be further evaluated by analyzing degradation rates (DRs) and the behavior of T_{80} as a function of area, which provides a quantitative assessment of the stability for the two active layers (Fig. 6e and f). The DR is calculated as the difference in the performance parameter (PCE) between the initial and final states, divided by the test duration (T_{80}), as explained in our previous studies.[77,78]

Overall, these results indicate that while efficiency losses upon area scaling are primarily governed by resistive and geometric limitations during operation, the intrinsic dark and photo-stability of spin-coated OSCs is not compromised at the centimeter scale. In contrast, PM6:Y7-based devices exhibit enhanced operational robustness with increasing area, reinforcing the viability of spin coating for intermediate-area OSC fabrication.

Experimental section

Materials

The indium tin oxide (ITO) patterned glass substrate with a resistivity of 15 Ω sq^{-1} was purchased from Yanko Shangsheng Business Co., Ltd. PDINO, PM6 (PBDB-T-2F) polymer donor and Y7 and L8-BO NFAs were purchased from One-Material Inc. Chlorobenzene and chloroform solvents, and 1,8-diiodooctane (DIO) and 1-chloronaphthalene (CN) additives, were obtained from Sigma-Aldrich. A high-purity silver (Ag, 99.99%) wire was obtained from Testbourne Ltd.

Solar cell fabrication

The fabrication of the conventional OSCs was based on the structure ITO/PEDOT:PSS/PM6:Y7 or PM6:L8-BO/PDINO/Ag. First, the pre-patterned ITO glass substrates were cleaned sequentially in deionized water with detergent and then ultrasonicated in high-purity solvents (acetone, methanol, and isopropanol) for 10 min each. Afterward, the cleaned ITO glass substrates were dried in an oven at 100 °C for 10 min and treated with ultraviolet light for 15 minutes to remove any organic residue and create a hydrophilic surface. Two spin-coating strategies were employed for material deposition: static and dynamic.

In the static approach, 200 μL of solution were dispensed over 3 s, moving the micropipette tip from the center toward the edges to ensure full coverage before initiating rotation. In the dynamic approach, 100 μL of solution were dispensed in a continuous stream at the substrate's center while already in motion. For the latter, the micropipette tip was maintained at a height of approximately 1 cm, with a deposition time of 2 s. The PEDOT:PSS solution was deposited onto the cleaned ITO substrates *via* static-spin-coating (acceleration of 4000 rpm s^{-1}) for 40 s. Following deposition, the films were annealed in air at 150 °C for 15 min. Subsequently, the substrates were transferred to a nitrogen-filled glove box for active layer deposition.

The active layer solutions were prepared as follows: the PM6:Y7 blend (1 : 1 wt%, 20 mg mL^{-1}) was dissolved in chlorobenzene (CB) with 0.5% (v/v) 1-chloronaphthalene (CN) and stirred for 3 h at 80 °C. The PM6:L8-BO blend (1 : 1.2 wt%, 17.6 mg mL^{-1}) was dissolved in chloroform (CF) with 0.25% (v/v) 1,8-diiodooctane (DIO) and stirred for 4 h at 40 °C.

For device fabrication, PM6:Y7 was deposited *via* static spin-coating at 1500 rpm (1500 rpm s^{-1} acceleration) for 40 s, followed by thermal annealing at 90 °C for 5 min. PM6:L8-BO was deposited *via* dynamic spin-coating at 2500 rpm (2500 rpm s^{-1} acceleration) for 40 s and annealed at 100 °C for 10 min. Then, the PDINO interlayer (1.5 mg mL^{-1} in methanol) was applied through static spin-coating at 3000 rpm for 30 s.

Finally, the substrates were transferred to an evaporation chamber integrated within the glove box, where a 100 nm silver (Ag) electrode was deposited under high vacuum ($<1 \times 10^{-6}$ mbar). The active area of the resulting devices ranged from 0.09 to 4 cm^2.

Solar cell characterization

The current density–voltage (*J–V*) characteristics of the devices under light and dark conditions were obtained at room temperature with a Keithley 2400 source-measure unit using a solar simulator (Abet Technologies model 11000 class type A, xenon arc). The solar simulator intensity calibration was performed with a Fraunhofer certified photovoltaic cell to obtain 100 mW cm^{-2} under the AM1.5 G spectrum. The EQE measurement was performed from 300 nm to 1000 nm using a Lasing IPCE-DC model system. The devices were analyzed for up to 2500 h under N_2 and under continuous illumination for over 1550 min following the ISOS D-1 and L-1 protocols.

Conclusions

In summary, we successfully fabricated OSCs with active areas ranging from 0.09 to 4 cm^2 using a spin-coating process, demonstrating the viability of this technique for intermediate-area OSC fabrication. The spin-coated active layers exhibit highly uniform thickness and low surface roughness across the device area, with comparable morphological characteristics at the center and edges, confirming that film inhomogeneity is not the dominant limitation upon upscaling. An active-area increase of 44 times was achieved while retaining power conversion efficiencies of 10.7% and 11.1% for PM6:L8-BO- and PM6:Y7-based devices, respectively, highlighting the robustness of the fabrication process.

Although this study focuses on PM6:Y7 and PM6:L8-BO as representative high-performance donor–acceptor systems, the dominant scaling losses identified here (due to increased series

resistance and lateral charge transport limitations) originate primarily from architectural and geometric constraints rather than blend-specific effects. As such, these resistive penalties are expected to be broadly relevant across solution-processed organic photovoltaic systems, consistent with previous reports on other donor–acceptor blends. This suggests that the main conclusions derived here are not limited to the specific materials studied but reflect more general scaling constraints in centimeter-scale organic solar cells.

The performance losses observed upon scaling are primarily attributed to resistive and geometric effects rather than intrinsic material or processing limitations. While the open-circuit voltage remains largely unaffected by device area, the reduction in short-circuit current density and fill factor is mainly governed by the increase in series resistance associated with lateral charge transport through the ITO electrode. Spatially resolved EQE and AFM analyses confirm that morphological non-uniformities play only a secondary role in efficiency degradation, reinforcing the conclusion that electrode-related resistive losses dominate at the centimeter scale.

A comprehensive stability analysis under ISOS-D-1 and ISOS-L-1 protocols reveals that device stability is not compromised by area upscaling. Under dark storage in an inert N_2 atmosphere (<0.1 ppm O_2 and H_2O), degradation proceeds slowly and is mainly driven by intrinsic electrical aging and interfacial processes involving metallic and organic layers, rather than by chemical decomposition of the photoactive materials. In this regime, the fill factor is the primary contributor to PCE decay, correlating with a gradual increase in series resistance. Under continuous illumination, all devices exhibit an initial burn-in phase followed by a slower degradation regime, with performance losses dominated by the evolution of J_{SC} and FF. Importantly, larger-area devices consistently display reduced degradation rates and longer T_{80} lifetimes under both dark and illuminated conditions.

Between the two systems studied, PM6:Y7-based devices exhibit superior operational stability compared to PM6:L8-BO, especially under continuous illumination. This work demonstrates that while efficiency losses during upscaling are mainly dictated by resistive limitations, the intrinsic photo- and dark stability of spin-coated OSCs is preserved and even enhanced at the centimeter scale. These findings provide important insights into the mechanisms governing large-area OSC performance and stability.

Author contributions

Angel Sacramento: investigation; data processing; formal analysis; methodology; validation; writing. Mohamed Samir: data processing and formal analysis. Osbel Almora: data processing; formal analysis and review. Amina Shehbaz: methodology and data processing. Lluis F. Marsal: review; funding acquisition; project administration.

Conflicts of interest

The authors declare that there are no conflicts of interest.

Data availability

The data that support the findings of this study are available on request from the corresponding author. The data are not publicly available due to privacy or ethical restrictions. Supplementary information (SI) is available. See DOI: https://doi.org/10.1039/d6ta01450j.

Acknowledgements

A. S. thanks the Ministry of Research and Universities, Department of Climate Action, Food and Rural Agenda and the Climate Fund of the Generalitat de Catalunya for funding the project Conversion of Energy in Sustainable Chemicals (CESC, 2023 CLIMA 00067). M. S. acknowledges the financial support from Programa Martí I Franquès. This work was further supported by the Spanish Ministerio de Ciencia e Innovación (MICINN/FEDER) under Grant PDI2021-128342OB-I00, by the Agency for Management of University and Research Grants (AGAUR) ref. 2021-SGR-00739, and by the Catalan Institution for Research and Advanced Studies (ICREA) under the ICREA Academia Award.

References

1 F. C. Krebs, *Sol. Energy Mater. Sol. Cells*, 2009, **93**, 394–412.
2 C. J. Brabec, S. Gowrisanker, J. J. M. Halls, D. Laird, S. Jia and S. P. Williams, *Adv. Mater.*, 2010, **22**, 3839–3856.
3 G. Li, R. Zhu and Y. Yang, *Nat. Photon.*, 2012, **6**, 153–161.
4 T. M. Eggenhuisen, Y. Galagan, A. F. K. V. Biezemans, T. M. W. L. Slaats, W. P. Voorthuijzen, S. Kommeren, S. Shanmugam, J. P. Teunissen, A. Hadipour, W. J. H. Verhees, S. C. Veenstra, M. J. J. Coenen, J. Gilot, R. Andriessen and W. A. Groen, *J. Mater. Chem. A*, 2015, **3**, 7255–7262.
5 W. Cardoso, S. Massardo, A. Zaffar, J. F. Basbus, S. Presto, A. Barbucci and M. Viviani, *Chem. Eng. Trans.*, 2025, **120**, 601–606.
6 M. A. Butt, *Coatings*, 2022, **12**, 1115.
7 Y. Jiang, K. Liu, F. Liu, G. Ran, M. Wang, T. Zhang, R. Xu, H. Liu, W. Zhang, Z. Wei, Y. Cui, X. Lu, J. Hou and X. Zhu, *Adv. Mater.*, 2025, **37**, 2500282.
8 K. Sun, Y. Wang, G. Zhang, C. Gao, X. Ling, J. Zheng, J. Che, C. Xie, Z. Wang, H. Hu, P. You, P. Han, S. Li and Y. Chen, *Adv. Mater.*, 2025, **37**, e09806.
9 O. Almora, A. O. Alvarez, D. Baran, C. I. Cabrera, L. A. Castriotta, B. Ehrler, S. Erten-Ela, K. Fukuda, F. Guo, J. Hauch, A. W. Y. Ho-Baillie, T. J. Jacobsson, R. A. J. Janssen, T. Kirchartz, M. A. Loi, R. R. Lunt, X. Mathew, J. Min, D. B. Mitzi, M. K. Nazeeruddin, A. F. Nogueira, U. W. Paetzold, N. G. Park, B. P. Rand, H. Snaith, T. Someya, C. Sprau, L. Sun, K. Forberich and C. J. Brabec, *Adv. Energy Mater.*, 2025, e05525.
10 A. S. Gertsen, M. F. Castro, R. R. Søndergaard and J. W. Andreasen, *Flexible Printed Electron.*, 2020, **5**, 014004.
11 X. Xiao, K. Lee and S. R. Forrest, *Appl. Phys. Lett.*, 2015, **106**, 213301.

12 L. Mao, L. Sun, B. Luo, Y. Jiang and Y. Zhou, *J. Mater. Chem. A*, 2018, **6**, 5817–5824.
13 P. Cheng and X. Zhan, *Chem. Soc. Rev.*, 2016, **45**, 2544–2582.
14 Y. Zhang, H. Xia, J. Yu, Y. Yang and G. Li, *Adv. Mater.*, 2025, **37**, 2504063.
15 J. C. Carrillo-Sendejas and J. L. Maldonado, *Appl. Energy*, 2025, **3**, 021501.
16 Y. Han, X. Chen, J. Wei, G. Ji, C. Wang, W. Zhao, J. Lai, W. Zha, Z. Li, L. Yan, H. Gu, Q. Luo, Q. Chen, L. Chen, J. Hou, W. Su and C. Ma, *Adv. Sci.*, 2019, **6**, 1901490.
17 C. Xie, B. Liu, C. Xiao, X. Liu, Y. Liu, Z. Cai, Y. Li, G. Lu and W. Li, *Chem. Eng. J.*, 2023, **461**, 142124.
18 X. Jiang, L. Sun, W. Wang, F. Qin, C. Xie, L. Hua and Y. Zhou, *J. Mater. Chem. A*, 2020, **8**, 69–76.
19 Y. Wang, J. Luke, A. Privitera, N. Rolland, C. Labanti, G. Londi, V. Lemaur, D. T. W. Toolan, A. J. Sneyd, S. Jeong, D. Qian, Y. Olivier, L. Sorace, J. Kim, D. Beljonne, Z. Li and A. J. Gillett, *Joule*, 2023, **7**, 810–829.
20 S. Shoaee, H. M. Luong, J. Song, Y. Zou, T. Q. Nguyen and D. Neher, *Adv. Mater.*, 2024, **36**, 2302005.
21 J. Zhang, W. Xu, H. Tian, Z. Liu and F. Zhang, *ChemPhotoChem*, 2024, **8**, e202300348.
22 M. Samir, E. Moustafa, O. Almora, M. Ramírez-Como, M. P. Montero-Rama, J. G. Sánchez, E. Palomares, J. Pallarès and L. F. Marsal, *ACS Appl. Mater. Interfaces*, 2024, **16**, 16317–16327.
23 A. Sacramento, J. L. Abad, M. Ramírez-Como, V. S. Balderrama and M. Estrada, *Sustain. Energy Fuels*, 2024, **8**, 103–112.
24 M. Ramírez-Como, E. Moustafa, M. Samir, A. A. A. Torimtubun, J. G. Sánchez, J. Pallarès and L. F. Marsal, *Sustain. Energy Fuels*, 2023, **7**, 3883–3892.
25 M. O. Reese, S. A. Gevorgyan, M. Jørgensen, E. Bundgaard, S. R. Kurtz, D. S. Ginley, D. C. Olson, M. T. Lloyd, P. Morvillo, E. A. Katz, A. Elschner, O. Haillant, T. R. Currier, V. Shrotriya, M. Hermenau, M. Riede, K. R. Kirov, G. Trimmel, T. Rath, O. Inganäs, F. Zhang, M. Andersson, K. Tvingstedt, M. Lira-Cantu, D. Laird, C. McGuiness, S. Gowrisanker, M. Pannone, M. Xiao, J. Hauch, R. Steim, D. M. DeLongchamp, R. Rösch, H. Hoppe, N. Espinosa, A. Urbina, G. Yaman-Uzunoglu, J. B. Bonekamp, A. J. J. M. Van-Breemen, C. Girotto, E. Voroshazi and F. C. Krebs, *Sol. Energy Mater. Sol. Cells*, 2011, **95**, 1253–1267.
26 K. D. Rosenthal, M. P. Hughes, B. R. Luginbuhl, N. A. Ran, A. Karki, S. J. Ko, H. Hu, M. Wang, H. Ade and T. Q. Nguyen, *Adv. Energy Mater.*, 2019, **9**, 1901077.
27 J. Widmer, M. Tietze, K. Leo and M. Riede, *Adv. Funct. Mater.*, 2013, **23**, 5814–5821.
28 A. Trindade and L. Pereira, *Int. J. Photoenergy*, 2017, **2017**, 1364152.
29 C. J. Brabec, A. Cravino, D. Meissner, N. S. Sariciftci, T. Fromherz, M. T. Rispens, L. Sanchez and J. C. Hummelen, *Adv. Funct. Mater.*, 2001, **11**, 374–380.
30 G. Wang, M. A. Adil, J. Zhang and Z. Wei, *Adv. Mater.*, 2019, **31**, 1805089.
31 S. Choi, W. J. Potscavage and B. Kippelen, *J. Appl. Phys.*, 2009, **106**, 054507.
32 V. Mihailetchi, L. Koster, J. Hummelen and P. Blom, *Phys. Rev. Lett.*, 2004, **93**, 216601.
33 N. Agrawal, M. Z. Ansari, A. Majumdar, R. Gahlot and N. Khare, *Sol. Energy Mater. Sol. Cells*, 2016, **157**, 960–965.
34 M. Islam, A. Kumar and A. Thakur, *J. Electron. Mater.*, 2021, **50**, 3603–3613.
35 J. Luke, Y. R. Jo, C. T. Lin, S. Hong, C. Balamurugan, J. Kim, B. Park, K. Lee, J. R. Durrant, S. Kwon, B. J. Kim and J. S. Kim, *J. Mater. Chem. A*, 2023, **11**, 1281–1289.
36 M. A. Green, *Solar Cells: Operating Principles, Technology, and System Applications*, Prentice Hall, 1981, p. 274.
37 T. Kirchartz, F. Deledalle, P. S. Tuladhar, J. R. Durrant and J. Nelson, *J. Phys. Chem. Lett.*, 2013, **4**, 2371–2376.
38 D. Lübke, P. Hartnagel, M. Hülsbeck and T. Kirchartz, *ACS Mater. Au*, 2023, **3**, 215–230.
39 U. Würfel, D. Neher, A. Spies and S. Albrecht, *Nat. Commun.*, 2015, **6**, 6951.
40 B. Guo, W. Li, X. Guo, X. Meng, W. Ma, M. Zhang and Y. Li, *Adv. Mater.*, 2017, **29**, 1702291.
41 S. Waheed, S. Pareek and S. Karak, *J. Renewable Sustainable Energy*, 2023, **15**, 013502.
42 D. Barreiro-Argüelles, G. Ramos-Ortiz, J. L. Maldonado, E. Pérez-Gutiérrez, D. Romero-Borja, M. A. Meneses-Nava and J. C. Nolasco, *Sol. Energy*, 2018, **163**, 510–518.
43 H. Jin, A. Armin, M. Hambsch, Q. Lin, P. L. Burn and P. Meredith, *Phys. Status Solidi A*, 2015, **212**, 2246–2254.
44 B. Usmani, R. Ranjan, R. K. Gupta and A. Garg, *Oxford Open Mater. Sci.*, 2024, **4**, itae005.
45 W. Pan, Y. Han, Z. Wang, C. Gong, J. Guo, J. Lin, Q. Luo, S. Yang and C. Q. Ma, *J. Mater. Chem. A*, 2021, **9**, 16889–16897.
46 G. Ji, W. Zhao, J. Wei, L. Yan, Y. Han, Q. Luo, S. Yang, J. Hou and C. Q. Ma, *J. Mater. Chem. A*, 2019, **7**, 212–220.
47 A. Armin, M. Velusamy, P. Wolfer, Y. Zhang, P. L. Burn, P. Meredith and A. Pivrikas, *ACS Photonics*, 2014, **1**, 173–181.
48 R. Betancur, A. Martínez-Otero, X. Elias, P. Romero-Gómez, S. Colodrero, H. Miguez and J. Martorell, *Sol. Energy Mater. Sol. Cells*, 2012, **104**, 87–91.
49 E. Moustafa, M. Méndez, J. G. Sánchez, J. Pallarès, E. Palomares and L. F. Marsal, *Adv. Energy Mater.*, 2023, **13**, 2203241.
50 C. He, Y. Pan, G. Lu, B. Wu, X. Xia, C. Q. Ma, Z. Chen, H. Zhu, X. Lu, W. Ma, L. Zuo and H. Chen, *Adv. Mater.*, 2022, **34**, 2203379.
51 H. Lee, C. Park, D. H. Sin, J. H. Park and K. Cho, *Adv. Mater.*, 2018, **30**, 1800453.
52 A. A. A. Torimtubun, M. Méndez, J. G. Sánchez, J. Pallarès, E. Palomares and L. F. Marsal, *Sustain. Energy Fuels*, 2021, **5**, 6498–6508.
53 E. Moustafa, J. Pallares and L. F. Marsal, *IEEE J. Electron Devices Soc.*, 2023, **11**, 642–649.
54 L. F. Hernández-García, L. Reséndiz, M. Ramírez-Como, A. Sacramento, V. Cabrera, M. Estrada, J. Pallarès and L. F. Marsal, *Mater. Renew. Sustain. Energy*, 2025, **14**, 1–14.

55 I. C. Flores, Y. L Casallas-Moreno, A. Sacramento, M. Ramírez-Como, M. Camacho-Reynoso, V. Cabrera, Y. Kudriavtsev, C. Rivera-Rodríguez and L. M. Reséndiz, *Mater. Res. Express*, 2024, **11**, 125103.
56 A. Sacramento, M. Ramírez-Como, V. S. Balderrama, J. G. Sánchez, J. Pallarès, L. F. Marsal and M. Estrada, *J. Mater. Chem. C*, 2021, **9**, 6518–6527.
57 E. Moustafa, M. Mendez, J. Pallares and L. F. Marsal, *Sol. Energy Mater. Sol. Cells*, 2022, **248**, 111985.
58 P. Chen, J. Huang, Z. Xiong and F. Li, *Org. Electron.*, 2013, **14**, 621–627.
59 L. M. Herz, *Annu. Rev. Phys. Chem.*, 2016, **67**, 65–89.
60 A. Sacramento, M. Ramírez-Como, V. S. Balderrama, S. I. Garduño, M. Estrada and L. F. Marsal, *IEEE J. Electron Devices Soc.*, 2020, **8**, 413–420.
61 L. D. Mario, D. G. Romero, H. Wang, E. K. Tekelenburg, S. Meems, T. Zaharia, G. Portale and M. A. Loi, *Adv. Mater.*, 2024, **36**, 2301404.
62 C. H. Peters, I. T. Sachs-Quintana, W. R. Mateker, T. Heumueller, J. Rivnay, R. Noriega, Z. M. Beiley, E. T. Hoke, A. Salleo and M. D. McGehee, *Adv. Mater.*, 2012, **24**, 663–668.
63 A. V. Kesavan, K. K. Khanum, S. Subbiahraj and P. C. Ramamurthy, *J. Phys. Chem. C*, 2019, **123**, 22699–22705.
64 J. Yuan, Y. Zhang, L. Zhou, G. Zhang, H. L. Yip, T. K. Lau, X. Lu, C. Zhu, H. Peng, P. A. Johnson, M. Leclerc, Y. Cao, J. Ulanski, Y. Li and Y. Zou, *Joule*, 2019, **3**, 1140–1151.
65 P. T. Tsai, K.-C. Lin, C. Y. Wu, C. H. Liao, M. C. Lin, Y. Q. Wong, H. F. Meng, P. C. Y. Chang, C. L. Wang, Y. F. Huang, S. F. Horng, H. W. Zan and Y. C. Chao, *ChemSusChem*, 2017, **10**, 2778–2787.
66 S. Zeiske, O. J. Sandberg, N. Zarrabi, W. Li, P. Meredith and A. Armin, *Nat. Commun.*, 2021, **12**, 3603.
67 L. Zesheng and Y. Lin, *Polym. Test.*, 2024, **132**, 108387.
68 C. Wöpke, C. Göhler, M. Saladina, X. Du, L. Nian, C. Greve, C. Zhu, K. M. Yallum, Y. J. Hofstetter, D. Becker-Koch, N. Li, T. Heumüller, I. Milekhin, D. R. T. Zahn, C. J. Brabec, N. Banerji, Y. Vaynzof, E. M. Herzig, R. C. I. MacKenzie and C. Deibel, *Nat. Commun.*, 2022, **13**, 3786.
69 V. Sangwan, Z. Martin, G. Li, F. Qin, S. Hadke, R. M. Pankow, W. C. Jeon, D. Zheng, Y. Cho, R. M. Young, K. L. Kohlstedt, M. R. Wasielewski, G. C. Schatz, A. Facchetti, M. C. Hersam and T. J. Marks, *J. Mater. Chem. A*, 2024, **12**, 21213–21229.
70 X. Xu, D. Li, J. Yuan, Y. Zhou and Y. Zou, *EnergyChem*, 2021, **3**, 100046.
71 M. B. Upama, M. Wright, M. A. Mahmud, N. K. Elumalai, A. M. Soufiani, D. Wang, C. Xua and A. Uddin, *Nanoscale*, 2017, **9**, 18788–18797.
72 A. Sacramento, V. S. Balderrama, M. Ramírez-Como, L. F. Marsal and M. Estrada, *Sol. Energy*, 2020, **198**, 419–426.
73 Q. Burlingame, X. Huang, X. Liu, C. Jeong, C. Coburn and S. R. Forrest, *Nat.*, 2019, **573**, 394–397.
74 B. Zhang, F. Yang and Y. Li, *Small Sci.*, 2023, **3**, 2300004.
75 H. T. Chien, P. W. Zach and B. Friedel, *ACS Appl. Mater. Interfaces*, 2017, **9**, 27754–27764.
76 T. W. David, N. Bristow, V. Stoichkov, H. Huang, G. Todeschini and J. Kettle, *Energies*, 2021, **14**, 6324.
77 M. Samir, O. Almora, A. Sacramento, J. Pallarès and L. F. Marsal, *Sol. RRL*, 2025, **9**, 2500397.
78 M. Samir, A. Sacramento, O. Almora, J. Pallarès and L. F. Marsal, *Sol. RRL*, 2024, **8**, 2400479.

